



HAL
open science

Nanoporous Titanium (Oxy)nitride Films as Broadband Solar Absorbers

Beatrice Bricchi, Luca Mascaretti, Simona Garattoni, Matteo Mazza, Matteo Ghidelli, Andrea Li Bassi, Alberto Naldoni

► **To cite this version:**

Beatrice Bricchi, Luca Mascaretti, Simona Garattoni, Matteo Mazza, Matteo Ghidelli, et al.. Nanoporous Titanium (Oxy)nitride Films as Broadband Solar Absorbers. ACS Applied Materials & Interfaces, 2022, 14 (16), pp.18453-18463. 10.1021/acsami.2c01185 . hal-03680643

HAL Id: hal-03680643

<https://hal.science/hal-03680643v1>

Submitted on 28 May 2022

HAL is a multi-disciplinary open access archive for the deposit and dissemination of scientific research documents, whether they are published or not. The documents may come from teaching and research institutions in France or abroad, or from public or private research centers.

L'archive ouverte pluridisciplinaire **HAL**, est destinée au dépôt et à la diffusion de documents scientifiques de niveau recherche, publiés ou non, émanant des établissements d'enseignement et de recherche français ou étrangers, des laboratoires publics ou privés.

Nanoporous titanium (oxy)nitride films as broadband solar absorbers

Beatrice R. Bricchi,^{a,†} Luca Mascaretti,^{b,†} Simona Garattoni,^a Matteo Mazza,^a Matteo Ghidelli,^c Alberto Naldoni,^{b,*} Andrea Li Bassi^{a,d,*}

^aMicro- and Nanostructured Materials Laboratory, Department of Energy, Politecnico di Milano, Via Ponzio 34/3, 20133 Milano, Italy

^bCzech Advanced Technology and Research Institute, Regional Centre of Advanced Technologies and Materials, Palacký University Olomouc, Šlechtitelů 27, 77900 Olomouc, Czech Republic

^cLaboratoire des Sciences des Procédés et des Matériaux (LSPM), CNRS, Université Sorbonne Paris Nord, 93430 Villetaneuse, France

^dCenter for Nanoscience and Technology – IIT@PoliMi, Via Giovanni Pascoli 70/3, 20133 Milano, Italy

† These authors contributed equally to this work.

Corresponding authors

* andrea.libassi@polimi.it

* alberto.naldoni@upol.cz

Abstract

Broadband absorption of solar light is a key aspect in many applications that involve an efficient conversion of solar energy to heat. Titanium nitride (TiN)-based materials, in form of periodic arrays of nanostructures or multilayers, can promote significant heat generation upon illumination thanks to their efficient light absorption and refractory character. In this work, pulsed laser deposition was chosen as a synthesis technique to tune the properties of TiN films from metallic bulk-like TiN to oxynitride hierarchical films featuring a nanoparticle-assembled tree-like morphology. The nanoporous hierarchical films exhibit strong broadband solar absorption ($\sim 90\%$ from the UV to the near infrared range) and could generate temperatures of ~ 475 °C under moderate light concentration (17 Suns). The high heat generation achieved by the tree-like films is ascribed to their peculiar morphology, structure and composition, which is favorable for light trapping and heat dissipation. These properties pave the way for the implementation of such films as solar absorber structures.

1. Introduction

The abundant and widespread availability of solar energy makes it a potential source for various sustainable energy conversion technologies. Solar-thermal conversion, for example, aims at transforming photons coming from the Sun into heat that could be used for residential, commercial or industrial applications.¹ An ideal solar absorber material should exhibit a unitary and omnidirectional absorption in the 250–2500 nm range of the electromagnetic spectrum, which can be achieved, for example, by metal-insulator-metal (MIM) multilayers.^{2,3} Additionally, broadband absorbers must convert light energy to heat without undergoing thermal degradation, which typically requires the use of refractory metals and oxides^{2,4} or carbon-based components.⁵

Titanium nitride (TiN) is a well-known refractory material employed in the complementary metal oxide semiconductor (CMOS) technology.⁶ TiN in the form of nanoparticles (NPs) or nanostructures exhibits similar plasmonic properties as Au, but it offers several advantages compared to the latter, including the compatibility with semiconductor technology,⁶ high thermal stability,^{7,8} and tunability of its plasmonic resonance by controlling its stoichiometry or crystalline quality.⁶ A further advantage of TiN is that its absorption peak can be extended towards the near-infrared (NIR) range and its optical losses can lead to higher photothermal heating compared to Au.^{9,10} Therefore, it is not surprising that this material has been considered in thermoplasmonics,^{11,12} in which light-to-heat conversion mediated by plasmonic structures is exploited for a wide range of applications,¹³ including solar steam generation,¹⁴ optical trapping¹⁵ and photothermal catalysis.^{16,17}

Broadband solar absorbers based on TiN can be realized by coupling multiple TiN nanostructures in different arrangements. For example, ordered arrays or periodic metamaterials made of nm-sized units, such as nanocavities,^{16,18} nanotubes¹⁹ and hollow squares,⁷ as well as non-periodic structures, such as nanodonuts²⁰ and nanopillars²¹, have been reported. These approaches can prevent thermal stresses in MIM multilayers due to the different thermal expansion coefficients in the materials. Apart from optimizing the thermal stability of the solar absorber, the achievement of a full absorption with a simple fabrication method is also challenging.²¹ A simple approach in this regard is represented by porous films made of NP assemblies grown on a flat substrate, in which broadband absorption can be achieved as a result of coupling among individual localized surface plasmon resonances (LSPRs) of the NPs and light-trapping effects (i.e., multiple reflections/scattering) promoted by the nm-scale porosity.^{22,23}

Compared to standard NP-assembled materials, TiN thin films can be synthesized by vacuum-phase methods including magnetron sputtering,^{24–26} glancing angle deposition,^{27,28} atomic layer deposition (ALD),^{29,30} and pulsed laser deposition (PLD).^{31,32} The latter, in particular, allows depositing virtually any material with high tunability of morphology and structure: compact layers,^{31,33} surface-supported NPs,^{34,35} hierarchical tree-like films,^{32,36,37} and ultra-porous foams^{38,39} can be obtained without the need of substrate heating. The latter is an important feature in terms of process energy utilization and usage of flexible substrates. In this work, we exploit the versatility of PLD to deposit TiN/TiO_xN_y nanostructured films in controlled atmosphere (from vacuum up to 100 Pa of N₂/H₂) to tune the morphology, structure and optical absorption, with the aim to realize broadband solar absorbers. Tree-like films deposited at 50 and 100 Pa, in particular, exhibited the highest optical absorption over the entire UV-visible-NIR range. All the investigated films were tested by non-contact thermal measurements under moderate solar irradiation. We show that the TiO_xN_y film deposited at 100 Pa produced the highest temperature of ~ 475 °C under 17 Suns, which was ascribed to its broadband optical absorption, unlike metallic-like TiN films deposited at pressures lower than 20 Pa. Our results open the way to the utilization of TiN-based broadband solar absorbers with controlled functional properties fabricated by PLD in solar-thermal devices.

2. Experimental methods

2.1. Samples preparation

PLD was performed in a vacuum chamber equipped with mass flow controllers to tune the partial gas pressure. Ablation was performed with a ns-pulsed laser (Nd:YAG, 2nd harmonic, $\lambda = 532$ nm) with pulse duration in the 5–7 ns range and repetition rate of 10 Hz. The laser pulses were focused on the target material through a viewport and the target of stoichiometric TiN (99.9% purity, Mateck GmbH) was mounted on a roto-translational manipulator ensuring a uniform ablation. The laser fluence on the target was set at 6.5 J cm^{-2} . Depositions were performed at room temperature and in vacuum ($\sim 10^{-3}$ Pa) or N₂/H₂ (95/5%) background gas mixture at the overall pressure equal to 10, 20, 50, and 100 Pa. Si (100), soda-lime glass and Ti plate substrates were cleaned in ultrasonic bath with isopropanol and mounted on a rotating sample holder placed head-on the target at a fixed distance of 50 mm. The deposition time was set at 2 hours.

2.2. Material characterization

The thin films morphology was evaluated by means of a field emission scanning electron microscopy (SEM, Zeiss SUPRA 40) on samples grown on silicon. The SEM microscope is equipped with an Oxford Instruments Si(Li) detector for energy-dispersive X-ray spectroscopy (EDX), which was employed to estimate the atomic percentage (at.%) of Ti, N and O in the films, by employing an accelerating voltage of 10 kV. The chemical composition of selected films was further analyzed by EDX mapping in a high-resolution transmission electron microscope (HRTEM, Titan G2) operated in scanning TEM mode (STEM) using a Super-X system with four silicon drift detectors (Bruker). STEM images were taken with a high-angle annular dark-field imaging (HAADF) detector (Fischione, model 3000). TEM lamellae were prepared with a FEI Helios Focused Ion Beam/SEM (Thermo Scientific). X-ray photoelectron spectroscopy (XPS) analysis was performed by a PHI 5000 VersaProbe II XPS system (Physical Electronics) with a monochromatized Al K α source (15 kV, 50 W) and a photon energy of 1486.7 eV. The crystalline structure of the films was investigated by X-ray diffraction (XRD) using a high-resolution X-ray powder diffractometer (PANalytical X'Pert Pro MPD) with Co K α radiation ($\lambda = 0.1789$ nm). The measurements were performed in Bragg-Brentano geometry in a 2θ range of 22° – 100° with a step size of 0.033° . Further qualitative information about stoichiometry/composition of the films was gained by Raman spectroscopy using a Renishaw InVia micro-Raman spectrometer equipped with a diode-pumped solid-state laser ($\lambda = 660$ nm, incident power on the sample of 0.94 mW, spectral resolution $\sim 3 \text{ cm}^{-1}$). The optical characterization of the films in the spectral range 250–2000 nm was evaluated by transmittance (T) and reflectance (R) spectra on samples deposited on soda-lime glass using a

PerkinElmer Lambda 1050 spectrophotometer equipped with an integrating sphere (150 mm diameter). In the spectral range 1330–25000 nm, transmittance and reflectance spectra on samples deposited on silicon were acquired by a vacuum Fourier-transform infrared (FTIR) Vertex 80v spectrophotometer.

2.3. Infrared thermal imaging

The heat generation produced by the films under irradiation was evaluated by measuring the temperature of the Ti substrate (thickness 0.125 mm) by a FLIR X6580sc infrared camera. The thermal camera was placed on the backside of the samples that were irradiated from the front side with a 1000 W solar simulator (Sciencetech A4 Lightline C250) equipped with an AM 1.5G filter and an aspheric condenser lens (ACL25416U, Thorlabs). The samples were kept in a custom-made vacuum cell equipped with a sapphire viewport on the front side (420GSG040-saphir, Pfeiffer Vacuum GmbH) and a CaF₂ viewport (VPCH512, Thorlabs) on the backside in a pure Ar atmosphere. The temperatures measured by the thermal camera were corrected by the spectral emissivity of the Ti plates measured by FTIR spectroscopy at room temperature and averaged in the sensitivity range of the thermal camera (2500–5500 nm).

3. Results and discussion

TiN films with different morphologies were synthesized by varying the background pressure during the deposition from vacuum up to 100 Pa of N₂/H₂ to favor Ti–N bonds formation during film growth. SEM cross-section and top-view micrographs are reported in Figure 1. The TiN film deposited in vacuum shows a compact and dense columnar structure (Figure 1a) and a smooth surface (Figure 1b). For the samples deposited at 10 and 20 Pa (Figures 1c–1f), the columns composing the film exhibit a slight deviation from a perfectly vertical growth direction with a consequent increase of porosity. A further increase of the background pressure during the deposition leads to the growth of a hierarchical nanoparticle assembly structure (Figures 1g and 1h), clearly visible for the film deposited at 100 Pa (Figures 1i–1j). As a consequence of the increase of film porosity with background pressure during deposition, the thickness of the films for a deposition duration of 2 h increased from 2.4 μm for the vacuum-deposited film up to 3, 4.5, 6, and 8.5 μm for the ones deposited at 10, 20, 50, and 100 Pa, respectively.

A morphological transition from compact to nonporous films by increasing the background gas pressure is typical of the PLD process.^{36,40} Upon the interaction of the focused pulsed laser on the target material in a controlled atmosphere, i.e., laser ablation, a plasma plume is generated and expands from the target toward the substrate. In low-pressure conditions, the ablated species possess high kinetic energy and lead to a compact or bulk-like growth. In high-pressure conditions, the background gas molecules and the ablated species undergo collisions, which decrease the kinetic energy of the latter and lead to a cluster-assembled growth regime.^{38,39} The peculiar hierarchical nanoparticle assembly (tree-like) morphology observed for the films deposited at 50 and 100 Pa (Figures 1g–1j) has been frequently observed for various oxides^{36,37,41} as well as for TiN.³² In the latter, similarly to the present case, by increasing the background gas deposition pressure a morphological evolution featuring a porosity and thickness increase in parallel with a density decrease was observed. However, a transition from compact to tree-like films was observed at 15–30 Pa, i.e., lower than in this case (50–100 Pa), which could be ascribed to the use of a different laser wavelength (i.e., $\lambda = 280$ nm) and a lower fluence (i.e., 3.4 J cm⁻²).

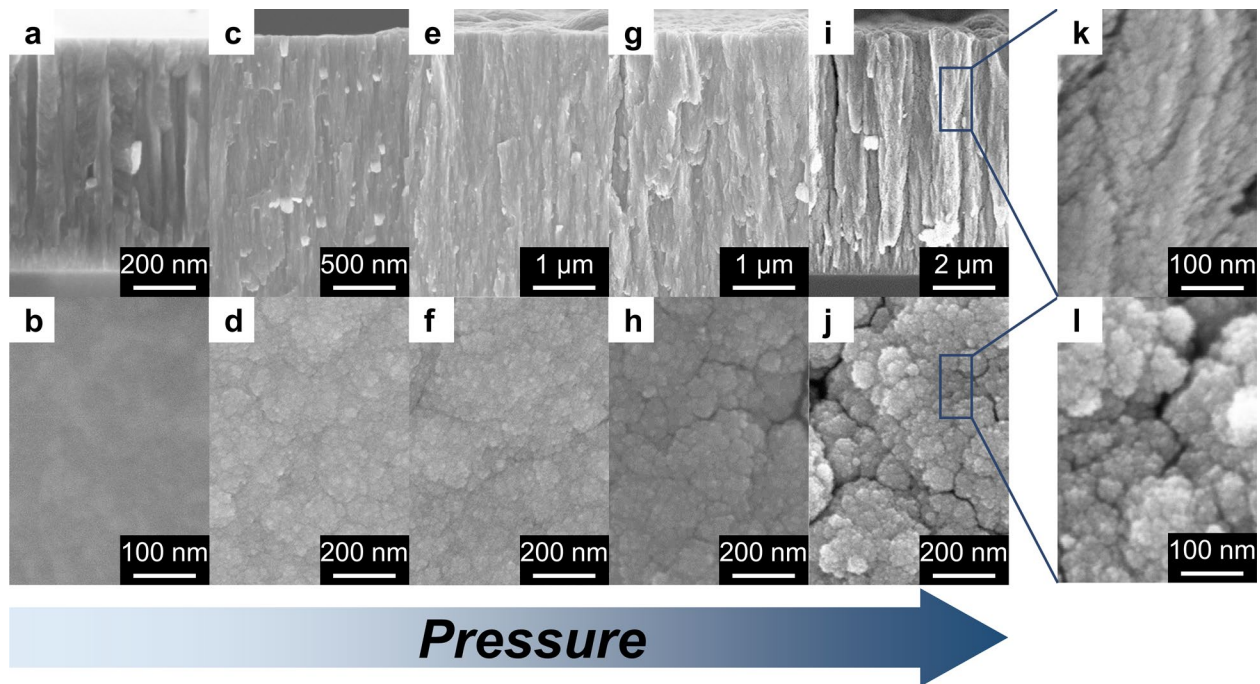


Figure 1. SEM cross-sectional (first row) and top views (second row) images of the films deposited (a,b) in vacuum, (c,d) at 10 Pa, (e,f) at 20 Pa, (g,h) at 50 Pa, and (i, j) at 100 Pa of N_2/H_2 ; (k) cross-sectional and (l) top view magnifications of the film deposited at 100 Pa.

The structural properties were investigated by XRD in Bragg-Brentano geometry, which is sensitive to the preferential orientation of crystalline domains along the film growth direction. The diffractograms for all the films exhibited the characteristic peaks of the cubic phase of TiN ($Fm-3m$ space group), but a remarkable change of texture and shift of the diffraction angles were found by increasing the background pressure during deposition. The vacuum-deposited film exhibited the (111) and (222) reflections at lower diffraction angles than the corresponding counterparts in bulk TiN. On the contrary, the film deposited at 10 Pa exhibited also the (200), which was the most intense in this case, (220) and (311) reflections (the latter slightly visible), all of them at higher diffraction angles than in the case of bulk TiN. By further increasing the deposition background pressure, all the peaks decreased in intensity and shifted to higher angles, while an amorphous background emerged at $P > 20$ Pa (Figure 2a). The peak shift effect can be better highlighted by evaluating the lattice constant a using the Bragg's law for cubic crystal system from the (111) reflections (vacuum, 10 Pa and 20 Pa) and (200) reflections (10–100 Pa), as shown in Figure 2b. Taking as reference value for bulk TiN $a_{TiN} = 4.2380 \text{ \AA}$, the vacuum-deposited film showed $a > a_{TiN}$. For all the other films, conversely, $a < a_{TiN}$ and the lattice constant decreased with the deposition pressure. Interestingly, for the films deposited at $P > 20$ Pa the lattice constant was lower than that of

cubic titanium monoxide, γ -TiO ($a_{\text{TiO}} = 4.182 \text{ \AA}$), which has the same rock-salt crystal structure as TiN. Furthermore, the average domain size (τ) along the film growth direction was evaluated through the broadening of the diffraction peaks by using the Scherrer equation on the (111) reflection for the films deposited in vacuum and 10–20 Pa, and on the (200) reflection for films deposited at 10–100 Pa (Figure 2c). For the film deposited in vacuum, $\tau \sim 18 \text{ nm}$; this value increases reaching a maximum for the film deposited at 10 Pa ($\tau \sim 46 \text{ nm}$ for the (111) reflection and $\tau \sim 32 \text{ nm}$ for (200) reflection), and finally decreases with the background pressure down to $\tau \sim 5 \text{ nm}$ for both the films deposited at 50 and 100 Pa.

XRD data could be interpreted in terms of the growth regimes induced by the increase of deposition background gas pressure. The features of the film deposited in vacuum ($a > a_{\text{TiN}}$) are consistent with two effects: on the one hand, a nitrogen sub-stoichiometry induced by non-stoichiometric transfer from the target and, therefore, nitrogen loss;^{42,43} on the other hand, in-plane compressive stresses due to highly energetic particles having a peening effect on the growing film.²⁴ The residual stresses indeed were retrieved by evaluating the macro-strain as $\varepsilon_{\text{macro}} = |a - a_{\text{ref}}| / a_{\text{ref}} = 0.015$, that is consistent with a compact film with compressive stress deposited by physical vapor deposition.^{26,44} By ablating the target in the presence of a N_2/H_2 background gas, instead, the species in the plume slowed down because of the collisions with the gas molecules. As a consequence, at 10 Pa a trade-off between in-plume cluster nucleation and sufficiently large kinetic energy of the ablated species probably promoted a good crystallization with small residual stresses ($\varepsilon_{\text{macro}} = 0.006$) and N incorporation in the growing film. A further pressure increase in the chamber promoted a less directional ablation plume and a low kinetic energy of the clusters formed in the plume. Therefore, a progressive decrease of the average domain size in parallel with amorphization of the film are expected.^{36,45} Another effect coming into play was a partial oxidation of the films due to residual impurities in the background gas. Previous studies, indeed, reported a decrease of the lattice parameter (down to 4.16 \AA) as well as of the average domain size (2.8 nm) by decreasing the flow rate of N_2 and increasing that of O_2 during magnetron sputtering experiments, thus producing titanium oxynitrides, i.e., TiO_xN_y .⁴⁶ For such materials, a lower lattice parameter compared to both standard TiN and TiO materials could be explained by the presence of ion vacancies.⁴⁷

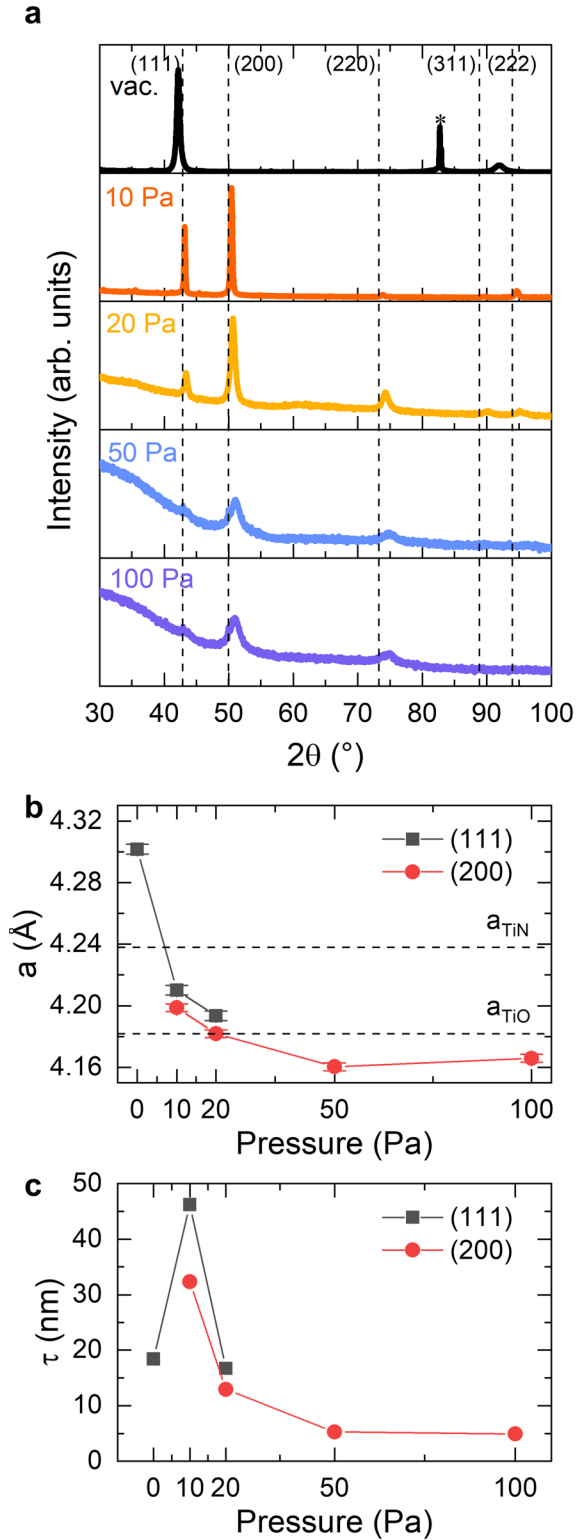


Figure 2. (a) XRD patterns of TiN films deposited in vacuum on Si substrate (main reflection marked with *) and at 10, 20, 50, and 100 Pa N_2/H_2 on glass substrates (vertical dashed lines: reference TiN peaks). (b) Lattice constant a and (c) average domain size (τ) evaluated for the (111) and (200) XRD reflections. The horizontal dashed lines in (b) correspond to the lattice constants for bulk TiN (4.238 Å)

and γ -TiO ($a_{\text{TiO}} = 4.182 \text{ \AA}$). Reference data for TiN taken from PDF database card no. 01-087-0633 and for TiO from ref⁴⁸.

The data presented in Figures 1 and 2 show the key role of the N_2/H_2 deposition pressure in controlling not only the morphology, but also the structure and the composition of the films. Since the latter itself deeply affects the functional properties of titanium nitride-based materials, a further compositional characterization was addressed by different techniques (Figure 3). EDX microanalysis was carried out to estimate the atomic content (% at.) of Ti, N and O in the films deposited at different pressure (Figure 3a) and the nitrogen to titanium ratio (N/Ti) was also considered (Figure 3b) to discern among sub-stoichiometric ($N/Ti < 1$), stoichiometric ($N/Ti = 1$) and over-stoichiometric ($N/Ti > 1$) films. For the film deposited in vacuum, the ratio N/Ti was ~ 0.4 (Ti $\sim 47\%$ at., N $\sim 18\%$ at.) with a high amount of oxygen (32% at.). For the film deposited at 10 Pa, oxygen was not detected and a condition of slight over-stoichiometry was found ($N/Ti \sim 1.1$). The film deposited at 20 Pa was characterized by a substantial amount of oxygen (O $\sim 33\%$ at.) and a decrease of N/Ti to ~ 0.8 . By further increasing the deposition pressure, the N/Ti ratio significantly decreased down to ~ 0.5 and the oxygen content increased up to $\sim 50\%$ at. It should be taken into account that EDX measurements were also performed on the TiN target, finding $N/Ti = 0.8$ and 13% at. O (Figure S1). Despite the intrinsic under-estimation of light atoms, such as nitrogen and oxygen, of the EDX technique, the compositional analysis confirmed the indirect observations from XRD (Figure 2). The relatively high oxygen content in the vacuum-deposited film and in the target could be simply ascribed to the formation of a native thin oxide surface layer due to air exposure.^{49,50} The same effect would also hold for the case of porous films; additionally, oxygen was likely included during the growth due to the deposition at high background gas pressures. More information in this regard was gained by Raman spectroscopy (Figure 3c). The vacuum-deposited film exhibited evident acoustic Raman bands ($\sim 200\text{--}300 \text{ cm}^{-1}$) without optical bands, which was ascribed to nitrogen vacancies and, therefore, under-stoichiometry (see Note S1 for more details on the interpretation of Raman spectra in TiN). The Raman spectra for the films deposited at 10 and 20 Pa, instead, were consistent with nearly-stoichiometric TiN. By further increasing the deposition pressure, the Raman spectra became broader, which could be explained by an increasing degree of amorphization and oxidation due to residual oxygen molecules in the chamber saturating the nitrogen vacancies.⁴⁶ In other words, the films deposited at 50 and 100 Pa were partially oxidized through the whole film thickness. To confirm this claim, further analysis was performed by STEM-EDX mapping on lamellae prepared from a film deposited at 100 Pa (Figures 3d–3g). The maps show that Ti, N and O are present all along the

tree-like structure. The measured elemental composition was Ti = 43.4% at., N = 23.5% at., and O = 33.1% at., with $N/Ti = 0.54$ in agreement with EDX microanalysis. Further information on the composition of this film was gained by XPS. The spectra revealed a rather low nitrogen amount ($\sim 10\%$ at.), while the binding energies of the peaks in the Ti 2p and O 1s regions were comparable to reduced titanium dioxide (see details in Figure S2 and Table S1). Therefore, the XPS data overall suggested an extensive surface oxidation for the film deposited at 100 Pa. It is possible to conclude that, while the films deposited at $P \leq 20$ Pa are consistent with titanium nitride materials with different stoichiometries, i.e., TiN_x , and limited (surface) oxidation, those deposited at $P \geq 50$ Pa correspond to titanium oxynitride materials, i.e., TiO_xN_y .

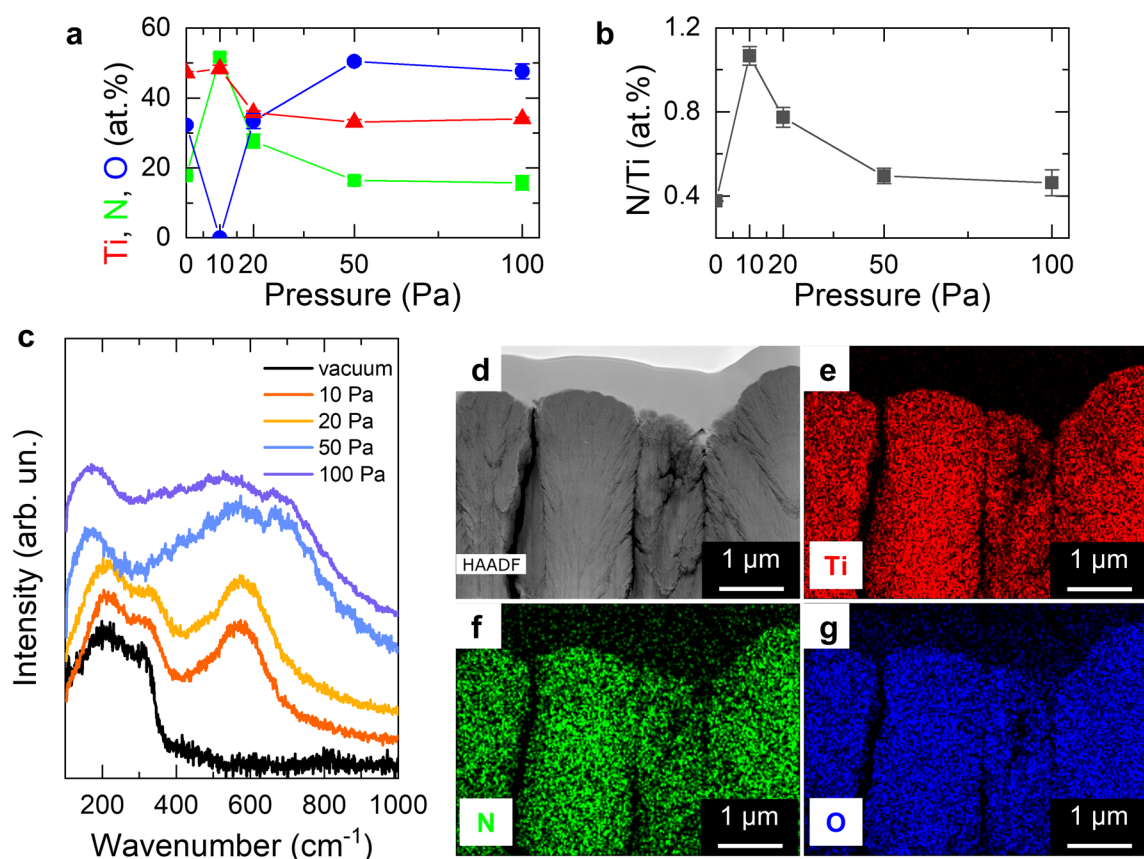


Figure 3. (a) Atomic percentage of Ti, N and O by EDX microanalysis and (b) N to Ti ratio (N/Ti) of the atomic percentage for film deposited from vacuum to 100 Pa N_2/H_2 (c) Raman spectra of the TiN films deposited in vacuum and at 10–100 Pa. (d) High-angle annular dark-field STEM (HAADF-STEM) image and corresponding EDX mapping of Ti (e), N (f) and O (g) for the film deposited at 100 Pa.

The morphological, structural and compositional evolution of the films with the increase of deposition pressure discussed above was accompanied by a change in the optical properties (Figure 4). Absorptance spectra were retrieved by transmittance ($T(\lambda)$) and reflectance ($R(\lambda)$) measurements (Figure S3) according to the formula $A(\lambda) = 1 - T(\lambda) - R(\lambda)$ (see Note S2 for details on the measurements in the different wavelength ranges and on data treatment). Figures 4a and 4b show the optical spectra in the ultraviolet-visible-near infrared (UV-vis-NIR, i.e., 250–2000 nm) range compared to the standard solar irradiance and in the medium-infrared (MIR, i.e., 1330–25000 nm) range, respectively. The absorptance monotonically increased and the overall behavior of the films dramatically changed by increasing the deposition pressure. In particular, the film deposited in vacuum showed zero transmittance (Figures S3a and S3b) and a well-defined reflectance minimum (Figures S3c and S3d) or absorptance maximum in the UV region of the electromagnetic spectrum (i.e., at 318 nm, Figure 4a). This behavior is very similar to that of bulk TiN, which exhibits a well-defined interband transition threshold at ~ 500 nm and a low absorption/high reflectance due to intraband transitions at longer wavelengths.⁶ For the films deposited at 10 and 20 Pa the absorption peak redshifted to 516 and 658 nm, respectively, and broadened, thus leading to a higher absorptance in the full UV–MIR range than the film deposited in vacuum. Additionally, these films exhibited a non-zero transmittance in the MIR range (maximum $\sim 10\%$ at ~ 10 μm , Figure S3b). Since the absorption maximum (or the reflectance minimum) position is associated to the plasma frequency of the film, its redshift can be explained with a change of charge carrier density, which implies a change of stoichiometry or composition.^{51,52} In this case, according to EDX analysis (Figures 2a–2b), a higher nitrogen or oxygen content contributed to the redshift of the absorption peak, thus decreasing the metallic character of the films. Moreover, the broadening of the absorption could be associated to a transition from a smooth film surface to a nanostructured one (Figure 1), which can promote light scattering and light trapping phenomena. This effect became more evident for the films deposited at 50 and 100 Pa, which exhibited a broadband absorption in the whole investigated range (Figures 4a and 4b). These films exhibited a non-zero transmittance at $\lambda > 530$ nm (Figure S3a) which increased up to $\sim 60\%$ at MIR wavelengths, then abruptly decreased to zero (Figure S3b). As a result, the absorptance exhibited broad maxima in the visible ($\lambda \sim 500$ nm), in the NIR ($\lambda \sim 1000$ nm) and in the MIR ($\lambda \sim 13000$ nm) ranges of the electromagnetic spectrum, with an absolute minimum at ~ 10000 nm. Various effects could explain such an optical behavior. The main contribution is likely due to oxygen incorporation in the films, thus featuring a TiO_xN_y composition, which is supported by EDX, Raman and XPS data (Figures 3 and S2). TiO_xN_y materials show indeed a non-zero transmittance^{46,53} and a more extended energy range for interband transitions involving the additional O 2p orbitals⁵⁴. On the other

hand, broadband absorption was also shown for highly substoichiometric TiO_x ²² and commercial TiN ²³ NPs assemblies and for TiN nanopillars.²¹ In all these cases, a superposition of individual localized surface plasmon resonances (LSPRs) of the individual units, i.e., plasmon hybridization,^{55,56} increased and broadened the overall absorption of the film. Yan *et al.* further showed that the porous nanostructure promoted light trapping due to multiple reflections and scattering of light as well as a reduced reflectance at the air-solid interface due to an effective graded refractive index layer.²² Similarly, in the present case, an increase of light scattering ability of the films with the morphological transition from compact to porous was assessed by retrieving the haze factor, i.e., the ratio between the diffuse and total components of the transmittance (Note S2), which increased with the deposition pressure for the films deposited at 50 and 100 Pa (Figure S3e).

To evaluate the overall performance of the films as solar absorbers, the spectrally averaged solar absorptance was calculated according to the formula⁵⁷

$$\bar{\alpha} = \frac{\int_{280}^{2000} A(\lambda)S_s(\lambda)d\lambda}{I_{solar}} \quad (1)$$

where $S_s(\lambda)$ is the spectral solar irradiance (AM 1.5G), I_{solar} is the total irradiance, and the calculation is performed in the investigated wavelengths range, i.e., 280–2000 nm. Figure 4c shows that this quantity monotonically increased with the deposition pressure. In particular, $\bar{\alpha}$ abruptly increased from ~ 0.29 for the film prepared in vacuum to ~ 0.61 for the film deposited at 10 Pa, and then it reached the maximum value of ~ 0.89 at the deposition pressure of 100 Pa, thus confirming the trend discussed above. The $\bar{\alpha}$ value found for the film deposited at 100 Pa is comparable to other solar absorbers reported in the literature, such as a 2D Ta photonic crystal ($\bar{\alpha} = 0.864$),⁵⁷ a $\text{Ti}/\text{Al}_2\text{O}_3/\text{Ta}$ plasmonic metamaterial ($\bar{\alpha} = 0.913$),⁵⁸ TiN nanopillars ($\bar{\alpha} = 0.94$),²¹ and TiN/TiN NPs/ SiO_2 ceramic layer ($\bar{\alpha} = 0.95$).²³ Hence, the data presented in Figure 4 highlight the possibility of achieving a broadband solar absorber behavior for the tree-like TiO_xN_y films deposited at high pressures. Compared to broadband absorbers made of complex TiN metamaterial structures,^{7,59} the hierarchical nanoporous TiO_xN_y films could represent a potential alternative thanks to their relatively simple preparation process.

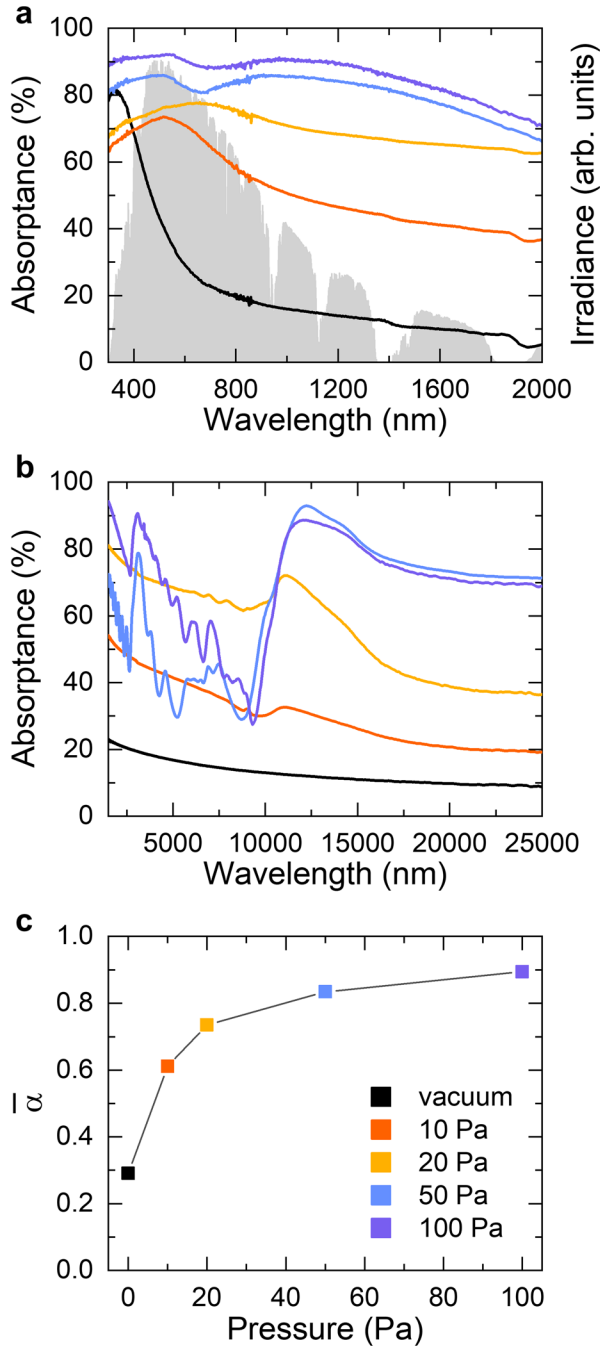


Figure 4. (a) Optical absorbance of the TiN films compared to the spectral solar irradiance (ASTM G173-03 AM 1.5 Global). (b) Optical absorbance in the MIR range retrieved by FTIR spectroscopy. (c) Spectrally averaged absorbance in the 280–2000 nm wavelength range. For all panels, the color legend is reported in (c).

The performance of the TiN/TiN_xO_y films for solar-thermal conversion applications was evaluated by non-contact thermal measurements under solar irradiation (Figure 5). The temperature reached under

solar-simulated light from 1.3 to 17 Suns (1 Sun = 100 mW cm⁻²) was measured with an infrared thermal camera pointing the back surface of the films deposited on titanium substrates (see Figure S4 for the experimental details and Figure S5 for a discussion on the substrate effect). The samples were kept in a home-made vacuum cell under inert Ar atmosphere to prevent surface oxidation and to allow multiple experiments under different irradiation conditions for extended periods of time.^{16,60,61} Figure 5a shows the temperature profiles during time under the maximum irradiation conditions (i.e., 17 Suns) for all the investigated films compared with an uncoated Ti substrate (see Figure S6 for the results for all the films under all irradiation conditions). It is possible to observe that the films heated up very quickly (i.e., in less than 10 s), contrarily to the bare Ti plate, and they reached a steady-state temperature after ~ 20 s. The steady-state temperature value measured at the end of the experiment, hereinafter labeled as T_{max} (maximum temperature) is shown for all the films under all the investigated solar intensities in Figure 5b. The generated temperature increased with the deposition pressure up to the maximum value of ~ 475 °C under 17 Suns irradiation for the film deposited at 100 Pa, which is a result comparable to the temperature generated by periodic TiN cylindrical nanocavities under the same moderately concentrated solar condition.¹⁶ This outcome is even more interesting considering that similar temperatures were reached by metallic nanoparticles array and TiN periodic nanostructures (i.e., nanotubes and trench) under laser irradiation with 10⁶-fold and 10⁴-fold greater power densities, respectively.^{19,62} Notably, the films did not undergo any degradation upon solar irradiation. Raman spectroscopy experiments (Figure S7), indeed, revealed only minor changes in the spectra compared to the pristine samples. While the experiments shown in Figures 6a and 6b were carried out in inert atmosphere, scale-up in environmental conditions could be realized by including a capping layer on top of the films, i.e., Al₂O₃ or Si₃N₄ by ALD.^{60,61}

To characterize the solar-thermal performance of the films, the spectrally averaged emissivity at each irradiation condition in correspondence of T_{max} was calculated as⁵⁷

$$\bar{\varepsilon}(T_{max}) = \frac{\int_{1330}^{25000} \varepsilon_{\lambda}(\lambda, T_0) E_b(\lambda, T_{max}) d\lambda}{\int_{1330}^{25000} E_b(\lambda, T_{max}) d\lambda} \quad (2)$$

In Equation (2), all the quantities are referred to the NIR–MIR range (i.e., the range investigated by FTIR measurements) because it is the typical range for thermal emission corresponding to surface temperatures of few hundreds of °C. $\varepsilon_{\lambda}(\lambda, T_0) = A_{FTIR}(\lambda, T_0)$ is the spectral emissivity according to the Kirchhoff's law of thermal radiation evaluated at room temperature (see a related discussion on the systematic errors

introduced by instrumental limitations of FTIR spectroscopy in Note S2), while $E_b(\lambda, T_{\max})$ is the black-body irradiance given by the Planck's law,

$$E_b(\lambda, T_{\max}) = \left(\frac{2\pi hc^2}{\lambda^5} \right) \frac{1}{\exp\left(\frac{hc}{\lambda k_B T_{\max}} \right) - 1} \quad (3)$$

where h is the Planck constant, c is the speed of light, and k_B is the Boltzmann constant. Figure 5c shows the values for $\bar{\varepsilon}(T_{\max})$ for all films under all irradiation conditions compared to the uncoated Ti substrate. The film deposited in vacuum exhibited a very low emittance (0.12–0.14) due to its highly metallic and reflective properties (Figure S3d). For all the other films, the emittance values fell in the interval 0.5–0.7, with the minimum $\bar{\varepsilon}(T_{\max}) = 0.51$ found for the film deposited at 50 Pa. The moderate difference in emittance values for the films deposited at 10–100 Pa (Figure 5c) compared to the dramatic increase of the spectrally averaged absorptance with the deposition pressure (Figure 4c) is due to the transparency window in the NIR range (up to $\sim 10 \mu\text{m}$) for the porous films (Figure S3b).

Taking into account the values of $\bar{\alpha}$ (Figure 4c) and $\bar{\varepsilon}(T_{\max})$ (Figure 5c), the thermal transfer efficiency was evaluated as¹

$$\eta_{th} = \bar{\alpha} - \bar{\varepsilon}(T_{\max}) \frac{\sigma(T_{\max}^4 - T_{amb}^4)}{CI_{solar}} \quad (4)$$

where $\sigma = 5.670367 \times 10^{-8} \text{ W m}^{-2} \text{ K}^{-4}$ is the Stefan-Boltzmann constant, $T_{amb} = 25 \text{ }^\circ\text{C}$ is the ambient temperature during the experiments, and C is the solar concentration factor (1.3–17). Figure 5d shows that the samples deposited at pressures ≥ 20 Pa outperformed the bare Ti substrate. The maximum thermal transfer efficiency was found for the film deposited at 100 Pa at 1.3 Suns ($\eta_{th} \sim 79\%$ at $T_{\max} \sim 54.9 \text{ }^\circ\text{C}$), and the efficiency values decreased with the irradiation intensity for all the investigated films. This is because the radiative losses are very limited at room temperature, but they follow a $\sim T^4$ dependence, thus making the emittance contribution increasingly more relevant at increasing temperatures. It is possible to note that under 17 Suns illumination, the film deposited at 50 Pa outperformed the one deposited at 100 Pa ($\eta_{th} \sim 35\%$ at $T_{\max} \sim 462 \text{ }^\circ\text{C}$ vs. $\eta_{th} \sim 22\%$ at $T_{\max} \sim 475 \text{ }^\circ\text{C}$) because of its lower absorptance in the NIR–MIR range (Figure 4b) and, therefore, lower emittance (Figure 5c). The performance of the hierarchical TiN_xO_y films at moderate temperature conditions is therefore lower than that of spectrally selective solar absorbers,^{23,57} which is not surprising since this work did not address a

control of the spectral emissivity of the TiN/TiN_xO_y films. In fact, the present results could be exploited to develop more advanced films limiting their emissivity in the MIR range. For example, compact/porous multi-layer structures could be realized in the same PLD process,^{23,63} or anti-reflection coatings could further be included.^{60,61} More complex architectures, such as nanopatterned surfaces,⁶⁴ could also be designed thanks to the possibility of depositing TiN_xO_y at room temperature on plastic substrates.

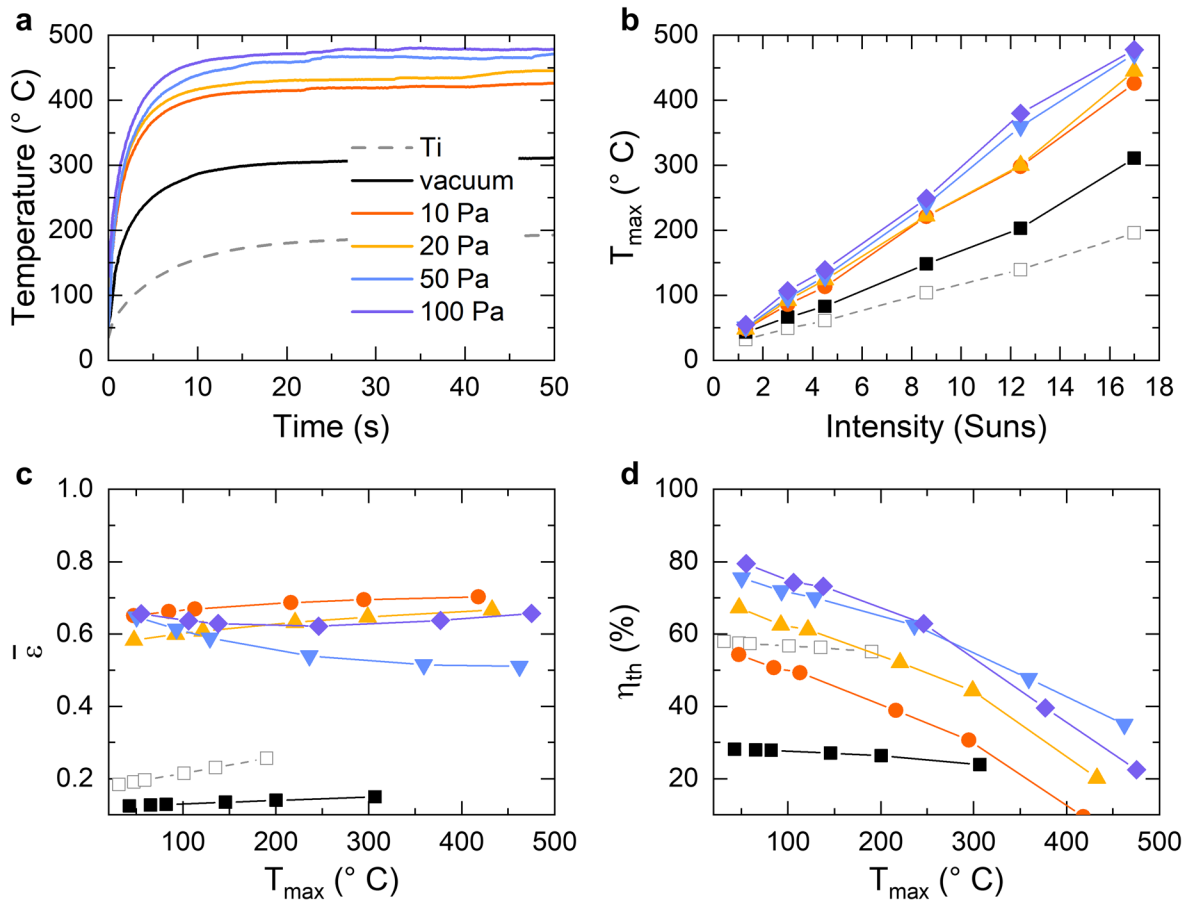


Figure 5. Solar-thermal performance of the investigated films. (a) Temperature profiles under 17 Suns as a function of time. (b) Maximum temperature (steady-state value at the end of each experiment) measured as a function of the solar power (1.3–17 Suns). (c) Spectrally averaged emittance and (d) thermal transfer efficiency as a function of the maximum temperature under irradiation. All panels report also the data for an uncoated titanium substrate.

Conclusions

Titanium (oxy)nitride films of tunable morphology, structure and composition were deposited by pulsed laser deposition at room temperature. By increasing the deposition background pressure from vacuum to 100 Pa, the films properties changed from bulk-like TiN to hierarchical nanoparticle assembly of TiO_xN_y . In particular, the hierarchical nanoporous films exhibited an ultra-fine nanocrystalline structure with a high degree of oxygen incorporation promoted by the high background gas (N_2/H_2) pressure during deposition. The light absorption of the films increased with the deposition pressure, thus allowing a broadband absorptance from the UV to the IR wavelength range. The films were studied as perspective candidates for solar-thermal applications by measuring the temperature produced under solar-simulated irradiation with moderate light concentration, which revealed the superior performance of the porous TiO_xN_y films (maximum temperature ~ 475 °C under 17 Suns) and resistance to oxidation. Further performance optimization could be addressed by simple design strategies thanks to the flexibility of pulsed laser deposition, such as by realizing compact/porous multilayers or by including anti-reflection oxide layers.

Associated content

The Supporting Information is available free of charge at...

Content of the SI: EDX microanalysis of the TiN target; high-resolution XPS spectra for the film deposited at 100 Pa; optical properties of the TiN films in the UV-vis-NIR and in the MIR ranges; details on the thermal camera measurements; top view SEM images of an uncoated Ti substrate and of all the investigated films on Ti substrates; temperature profiles under solar irradiation; Raman spectra before and after solar irradiation for all the investigated films; details on XPS peak fitting for the film deposited at 100 Pa; details on Raman spectroscopy experiments; details on optical spectroscopy experiments.

Author information

Corresponding authors

Andrea Li Bassi: Micro- and Nanostructured Materials Laboratory, Department of Energy, Politecnico di Milano, Via Ponzio 34/3, 20133 Milano, Italy; Center for Nanoscience and Technology – IIT@PoliMi, Via Giovanni Pascoli 70/3, 20133 Milano, Italy; orcid: 0000-0002-1265-4971; e-mail: andrea.libassi@polimi.it.

Alberto Naldoni: Regional Centre of Advanced Technologies and Materials, Czech Advanced Technology and Research Institute, Palacký University Olomouc, Šlechtitelů 27, 77900 Olomouc, Czech Republic; orcid:0000-0001-5932-2125.

Authors

Beatrice R. Bricchi: Micro- and Nanostructured Materials Laboratory, Department of Energy, Politecnico di Milano, Via Ponzio 34/3, 20133 Milano, Italy; orcid: 0000-0002-4107-7106;

Luca Mascaretti: Czech Advanced Technology and Research Institute, Regional Centre of Advanced Technologies and Materials, Palacký University Olomouc, Šlechtitelů 27, 77900 Olomouc, Czech Republic; orcid: 0000-0001-8997-7018;

Simona Garattoni: Micro- and Nanostructured Materials Laboratory, Department of Energy, Politecnico di Milano, Via Ponzio 34/3, 20133 Milano, Italy;

Matteo Mazza: Micro- and Nanostructured Materials Laboratory, Department of Energy, Politecnico di Milano, Via Ponzio 34/3, 20133 Milano, Italy;

Matteo Ghidelli: Laboratoire des Sciences des Procédés et des Matériaux (LSPM), CNRS, Université Sorbonne Paris Nord, 93430 Villetaneuse, France; orcid: 0000-0001-6057-9040;

Notes

The authors declare no competing financial interest.

Acknowledgments

L. M. and A. N. acknowledge support of the Ministry of Education, Youth and Sports of the Czech Republic through the Operational Programme Research, Development and Education – European Regional Development Fund, project no. CZ.02.1.01/0.0/0.0/15_003/0000416, and the Czech Science Foundation (GACR) through the project no. 20-17636S. The authors also thank Ondřej Tomanec for TEM and EDS measurements, Seyyedmohammadhossein Hejazi for XRD measurements, Veronika Šedajová for XPS measurements, and Filip Münz for his aid with FTIR measurements. The authors acknowledge CzechNanoLab Research Infrastructure supported by MEYS CR (LM2018110).

References

- (1) Weinstein, L. A.; Loomis, J.; Bhatia, B.; Bierman, D. M.; Wang, E. N.; Chen, G. Concentrating Solar Power. *Chem. Rev.* **2015**, *115* (23), 12797–12838. <https://doi.org/10.1021/acs.chemrev.5b00397>.
- (2) Deng, H.; Li, Z.; Stan, L.; Rosenmann, D.; Czaplewski, D.; Gao, J.; Yang, X. Broadband Perfect Absorber Based on One Ultrathin Layer of Refractory Metal. *Opt. Lett.* **2015**, *40* (11), 2592–2595. <https://doi.org/10.1364/OL.40.002592>.

- (3) Kajtár, G.; Kafesaki, M.; Economou, E. N.; Soukoulis, C. M. Theoretical Model of Homogeneous Metal–Insulator–Metal Perfect Multi-Band Absorbers for the Visible Spectrum. *J. Phys. Appl. Phys.* **2016**, *49* (5), 055104. <https://doi.org/10.1088/0022-3727/49/5/055104>.
- (4) Chirumamilla, M.; Roberts, A. S.; Ding, F.; Wang, D.; Kristensen, P. K.; Bozhevolnyi, S. I.; Pedersen, K. Multilayer Tungsten-Alumina-Based Broadband Light Absorbers for High-Temperature Applications. *Opt. Mater. Express* **2016**, *6* (8), 2704–2714. <https://doi.org/10.1364/OME.6.002704>.
- (5) Lenert, A.; Bierman, D. M.; Nam, Y.; Chan, W. R.; Celanović, I.; Soljačić, M.; Wang, E. N. A Nanophotonic Solar Thermophotovoltaic Device. *Nat. Nanotechnol.* **2014**, *9* (2), 126–130. <https://doi.org/10.1038/nnano.2013.286>.
- (6) Patsalas, P.; Kalfagiannis, N.; Kassavetis, S.; Abadias, G.; Bellas, D. V.; Lekka, Ch.; Lidorikis, E. Conductive Nitrides: Growth Principles, Optical and Electronic Properties, and Their Perspectives in Photonics and Plasmonics. *Mater. Sci. Eng. R Rep.* **2018**, *123*, 1–55. <https://doi.org/10.1016/j.mser.2017.11.001>.
- (7) Li, W.; Guler, U.; Kinsey, N.; Naik, G. V.; Boltasseva, A.; Guan, J.; Shalaev, V. M.; Kildishev, A. V. Refractory Plasmonics with Titanium Nitride: Broadband Metamaterial Absorber. *Adv. Mater.* **2014**, *26* (47), 7959–7965. <https://doi.org/10.1002/adma.201401874>.
- (8) Krekeler, T.; Rout, S. S.; Krishnamurthy, G. V.; Störmer, M.; Arya, M.; Ganguly, A.; Sutherland, D. S.; Bozhevolnyi, S. I.; Ritter, M.; Pedersen, K.; Petrov, A. Y.; Eich, M.; Chirumamilla, M. Unprecedented Thermal Stability of Plasmonic Titanium Nitride Films up to 1400 °C. *Adv. Opt. Mater.* **2021**, *9* (16), 2100323. <https://doi.org/10.1002/adom.202100323>.
- (9) Guler, U.; Shalaev, V. M.; Boltasseva, A. Nanoparticle Plasmonics: Going Practical with Transition Metal Nitrides. *Mater. Today* **2015**, *18* (4), 227–237. <https://doi.org/10.1016/j.mattod.2014.10.039>.
- (10) Ishii, S.; Shinde, S. L.; Nagao, T. Nonmetallic Materials for Plasmonic Hot Carrier Excitation. *Adv. Opt. Mater.* **2019**, *7* (1), 1800603. <https://doi.org/10.1002/adom.201800603>.
- (11) Baffou, G.; Quidant, R. Thermo-Plasmonics: Using Metallic Nanostructures as Nano-Sources of Heat. *Laser Photonics Rev.* **2013**, *7* (2), 171–187. <https://doi.org/10.1002/lpor.201200003>.
- (12) Baffou, G.; Cichos, F.; Quidant, R. Applications and Challenges of Thermoplasmonics. *Nat. Mater.* **2020**, *19* (9), 946–958. <https://doi.org/10.1038/s41563-020-0740-6>.
- (13) Naldoni, A.; Shalaev, V. M.; Brongersma, M. L. Applying Plasmonics to a Sustainable Future. *Science* **2017**, *356* (6341), 908–909. <https://doi.org/10.1126/science.aan5802>.
- (14) Neumann, O.; Urban, A. S.; Day, J.; Lal, S.; Nordlander, P.; Halas, N. J. Solar Vapor Generation Enabled by Nanoparticles. *ACS Nano* **2013**, *7* (1), 42–49. <https://doi.org/10.1021/nn304948h>.
- (15) Ndukaife, J. C.; Kildishev, A. V.; Nnanna, A. G. A.; Shalaev, V. M.; Wereley, S. T.; Boltasseva, A. Long-Range and Rapid Transport of Individual Nano-Objects by a Hybrid Electrothermoplasmonic Nanotweezer. *Nat. Nanotechnol.* **2016**, *11* (1), 53–59. <https://doi.org/10.1038/nnano.2015.248>.
- (16) Naldoni, A.; Kudyshev, Z. A.; Mascaretti, L.; Sarmah, S. P.; Rej, S.; Froning, J. P.; Tomanec, O.; Yoo, J. E.; Wang, D.; Kment, Š.; Montini, T.; Fornasiero, P.; Shalaev, V. M.; Schmuki, P.; Boltasseva, A.; Zbořil, R. Solar Thermoplasmonic Nanofurnace for High-Temperature Heterogeneous Catalysis. *Nano Lett.* **2020**, *20* (5), 3663–3672. <https://doi.org/10.1021/acs.nanolett.0c00594>.
- (17) Zhou, L.; Martirez, J. M. P.; Finzel, J.; Zhang, C.; Swearer, D. F.; Tian, S.; Robotjazi, H.; Lou, M.; Dong, L.; Henderson, L.; Christopher, P.; Carter, E. A.; Nordlander, P.; Halas, N. J. Light-Driven Methane Dry Reforming with Single Atomic Site Antenna-Reactor Plasmonic Photocatalysts. *Nat. Energy* **2020**, *5* (1), 61–70. <https://doi.org/10.1038/s41560-019-0517-9>.

- (18) Mascaretti, L.; Schirato, A.; Zbořil, R.; Kment, Š.; Schmuki, P.; Alabastri, A.; Naldoni, A. Solar Steam Generation on Scalable Ultrathin Thermoplasmonic TiN Nanocavity Arrays. *Nano Energy* **2021**, *83*, 105828. <https://doi.org/10.1016/j.nanoen.2021.105828>.
- (19) Ishii, S.; Higashino, M.; Goya, S.; Shkondin, E.; Tanaka, K.; Nagao, T.; Takayama, O.; Murai, S. Extreme Thermal Anisotropy in High-Aspect-Ratio Titanium Nitride Nanostructures for Efficient Photothermal Heating. *Nanophotonics* **2021**, *10* (5), 1487–1494. <https://doi.org/10.1515/nanoph-2020-0569>.
- (20) Thi Le, T.-L.; Nguyen, L. T.; Nguyen, H.-H.; Nghia, N. V.; Vuong, N. M.; Hieu, H. N.; Thang, N. V.; Le, V. T.; Nguyen, V. H.; Lin, P.-C.; Yadav, A.; Madarevic, I.; Janssens, E.; Bui, H. V.; Ngoc, L. L. T. Titanium Nitride Nanodonuts Synthesized from Natural Ilmenite Ore as a Novel and Efficient Thermoplasmonic Material. *Nanomaterials* **2021**, *11* (1), 76. <https://doi.org/10.3390/nano11010076>.
- (21) Chirumamilla, M.; Chirumamilla, A.; Yang, Y.; Roberts, A. S.; Kristensen, P. K.; Chaudhuri, K.; Boltasseva, A.; Sutherland, D. S.; Bozhevolnyi, S. I.; Pedersen, K. Large-Area Ultrabroadband Absorber for Solar Thermophotovoltaics Based on 3D Titanium Nitride Nanopillars. *Adv. Opt. Mater.* **2017**, *5* (22), 1700552. <https://doi.org/10.1002/adom.201700552>.
- (22) Yan, J.; Liu, P.; Ma, C.; Lin, Z.; Yang, G. Plasmonic Near-Touching Titanium Oxide Nanoparticles to Realize Solar Energy Harvesting and Effective Local Heating. *Nanoscale* **2016**, *8* (16), 8826–8838. <https://doi.org/10.1039/C6NR01295G>.
- (23) Li, Y.; Lin, C.; Wu, Z.; Chen, Z.; Chi, C.; Cao, F.; Mei, D.; Yan, H.; Tso, C. Y.; Chao, C. Y. H.; Huang, B. Solution-Processed All-Ceramic Plasmonic Metamaterials for Efficient Solar–Thermal Conversion over 100–727 °C. *Adv. Mater.* **2021**, *33* (1), 2005074. <https://doi.org/10.1002/adma.202005074>.
- (24) Patsalas, P.; Logothetidis, S. Optical, Electronic, and Transport Properties of Nanocrystalline Titanium Nitride Thin Films. *J. Appl. Phys.* **2001**, *90* (9), 4725–4734. <https://doi.org/10.1063/1.1403677>.
- (25) Reddy, H.; Guler, U.; Kudyshev, Z.; Kildishev, A. V.; Shalaev, V. M.; Boltasseva, A. Temperature-Dependent Optical Properties of Plasmonic Titanium Nitride Thin Films. *ACS Photonics* **2017**, *4* (6), 1413–1420. <https://doi.org/10.1021/acsphotonics.7b00127>.
- (26) Mascaretti, L.; Barman, T.; Bricchi, B. R.; Münz, F.; Li Bassi, A.; Kment, Š.; Naldoni, A. Controlling the Plasmonic Properties of Titanium Nitride Thin Films by Radiofrequency Substrate Biasing in Magnetron Sputtering. *Appl. Surf. Sci.* **2021**, *554*, 149543. <https://doi.org/10.1016/j.apsusc.2021.149543>.
- (27) Khan, R. K.; Farghaly, A. A.; Silva, T. A.; Ye, D.; Collinson, M. M. Gold-Nanoparticle-Decorated Titanium Nitride Electrodes Prepared by Glancing-Angle Deposition for Sensing Applications. *ACS Appl. Nano Mater.* **2019**, *2* (3), 1562–1569. <https://doi.org/10.1021/acsanm.8b02354>.
- (28) Jen, Y.-J.; Lin, M.-J.; Cheang, H.-L.; Chan, T.-L. Obliquely Deposited Titanium Nitride Nanorod Arrays as Surface-Enhanced Raman Scattering Substrates. *Sensors* **2019**, *19* (21), 4765. <https://doi.org/10.3390/s19214765>.
- (29) Langereis, E.; Heil, S. B. S.; van de Sanden, M. C. M.; Kessels, W. M. M. In Situ Spectroscopic Ellipsometry Study on the Growth of Ultrathin TiN Films by Plasma-Assisted Atomic Layer Deposition. *J. Appl. Phys.* **2006**, *100* (2), 023534. <https://doi.org/10.1063/1.2214438>.
- (30) Van Bui, H.; Kovalgin, A. Y.; Wolters, R. A. M. On the Difference between Optically and Electrically Determined Resistivity of Ultra-Thin Titanium Nitride Films. *Appl. Surf. Sci.* **2013**, *269*, 45–49. <https://doi.org/10.1016/j.apsusc.2012.09.074>.
- (31) Sugavaneshwar, R. P.; Ishii, S.; Dao, T. D.; Ohi, A.; Nabatame, T.; Nagao, T. Fabrication of Highly Metallic TiN Films by Pulsed Laser Deposition Method for Plasmonic Applications. *ACS Photonics* **2018**, *5* (3), 814–819. <https://doi.org/10.1021/acsphotonics.7b00942>.

- (32) Perego, A.; Giuffredi, G.; Mazzolini, P.; Colombo, M.; Brescia, R.; Prato, M.; Sabarirajan, D. C.; Zenyuk, I. V.; Bossola, F.; Dal Santo, V.; Casalegno, A.; Di Fonzo, F. Hierarchical TiN Nanostructured Thin Film Electrode for Highly Stable PEM Fuel Cells. *ACS Appl. Energy Mater.* **2019**, *2* (3), 1911–1922. <https://doi.org/10.1021/acsaem.8b02030>.
- (33) Kölbach, M.; Harbauer, K.; Ellmer, K.; van de Krol, R. Elucidating the Pulsed Laser Deposition Process of BiVO₄ Photoelectrodes for Solar Water Splitting. *J. Phys. Chem. C* **2020**, *124* (8), 4438–4447. <https://doi.org/10.1021/acs.jpcc.9b11265>.
- (34) Misra, S.; Li, L.; Jian, J.; Huang, J.; Wang, X.; Zemlyanov, D.; Jang, J.-W.; Ribeiro, F. H.; Wang, H. Tailorable Au Nanoparticles Embedded in Epitaxial TiO₂ Thin Films for Tunable Optical Properties. *ACS Appl. Mater. Interfaces* **2018**, *10* (38), 32895–32902. <https://doi.org/10.1021/acsaem.8b12210>.
- (35) Ghidelli, M.; Mascaretti, L.; Bricchi, B. R.; Zapelli, A.; Russo, V.; Casari, C. S.; Li Bassi, A. Engineering Plasmonic Nanostructured Surfaces by Pulsed Laser Deposition. *Appl. Surf. Sci.* **2018**, *434*, 1064–1073. <https://doi.org/10.1016/j.apsusc.2017.11.025>.
- (36) Mahjouri-Samani, M.; Tian, M.; Poretzky, A. A.; Chi, M.; Wang, K.; Duscher, G.; Rouleau, C. M.; Eres, G.; Yoon, M.; Lasseter, J.; Xiao, K.; Geohegan, D. B. Nonequilibrium Synthesis of TiO₂ Nanoparticle “Building Blocks” for Crystal Growth by Sequential Attachment in Pulsed Laser Deposition. *Nano Lett.* **2017**, *17* (8), 4624–4633. <https://doi.org/10.1021/acs.nanolett.7b01047>.
- (37) Noh, J. H.; Park, J. H.; Han, H. S.; Kim, D. H.; Han, B. S.; Lee, S.; Kim, J. Y.; Jung, H. S.; Hong, K. S. Aligned Photoelectrodes with Large Surface Area Prepared by Pulsed Laser Deposition. *J. Phys. Chem. C* **2012**, *116* (14), 8102–8110. <https://doi.org/10.1021/jp211233s>.
- (38) Mascaretti, L.; Nioretini, A.; Bricchi, B. R.; Ghidelli, M.; Naldoni, A.; Caramori, S.; Li Bassi, A.; Berardi, S. Syngas Evolution from CO₂ Electroreduction by Porous Au Nanostructures. *ACS Appl. Energy Mater.* **2020**, *3* (5), 4658–4668. <https://doi.org/10.1021/acsaem.0c00301>.
- (39) Maffini, A.; Pazzaglia, A.; Dellasega, D.; Russo, V.; Passoni, M. Growth Dynamics of Pulsed Laser Deposited Nanofoams. *Phys. Rev. Mater.* **2019**, *3* (8), 083404. <https://doi.org/10.1103/PhysRevMaterials.3.083404>.
- (40) Geohegan, D. B.; Poretzky, A. A. Dynamics of Laser Ablation Plume Penetration through Low Pressure Background Gases. *Appl. Phys. Lett.* **1995**, *67* (2), 197–199. <https://doi.org/10.1063/1.114665>.
- (41) Gondoni, P.; Mazzolini, P.; Russo, V.; Petrozza, A.; Srivastava, A. K.; Li Bassi, A.; Casari, C. S. Enhancing Light Harvesting by Hierarchical Functionally Graded Transparent Conducting Al-Doped ZnO Nano- and Mesoarchitectures. *Sol. Energy Mater. Sol. Cells* **2014**, *128*, 248–253. <https://doi.org/10.1016/j.solmat.2014.05.035>.
- (42) Schou, J. Physical Aspects of the Pulsed Laser Deposition Technique: The Stoichiometric Transfer of Material from Target to Film. *Appl. Surf. Sci.* **2009**, *255* (10), 5191–5198. <https://doi.org/10.1016/j.apsusc.2008.10.101>.
- (43) Canulescu, S.; Döbeli, M.; Yao, X.; Lippert, T.; Amoroso, S.; Schou, J. Nonstoichiometric Transfer during Laser Ablation of Metal Alloys. *Phys. Rev. Mater.* **2017**, *1* (7), 073402. <https://doi.org/10.1103/PhysRevMaterials.1.073402>.
- (44) Patsalas, P.; Gravalidis, C.; Logothetidis, S. Surface Kinetics and Subplantation Phenomena Affecting the Texture, Morphology, Stress, and Growth Evolution of Titanium Nitride Films. *J. Appl. Phys.* **2004**, *96* (11), 6234–6246. <https://doi.org/10.1063/1.1811389>.
- (45) Leichtweiss, T.; Henning, R. A.; Koettgen, J.; Schmidt, R. M.; Holländer, B.; Martin, M.; Wuttig, M.; Janek, J. Amorphous and Highly Nonstoichiometric Titania (TiO_x) Thin Films Close to Metal-like Conductivity. *J. Mater. Chem. A* **2014**, *2* (18), 6631–6640. <https://doi.org/10.1039/C3TA14816E>.

- (46) Trenczek-Zajac, A.; Radecka, M.; Zakrzewska, K.; Brudnik, A.; Kusior, E.; Bourgeois, S.; de Lucas, M. C. M.; Imhoff, L. Structural and Electrical Properties of Magnetron Sputtered Ti(ON) Thin Films: The Case of TiN Doped in Situ with Oxygen. *J. Power Sources* **2009**, *194* (1), 93–103. <https://doi.org/10.1016/j.jpowsour.2008.12.112>.
- (47) Sluban, M.; Umek, P.; Jagličić, Z.; Buh, J.; Šmitek, P.; Mrzel, A.; Bittencourt, C.; Guttman, P.; Delville, M.-H.; Mihailović, D.; Arčon, D. Controlling Disorder and Superconductivity in Titanium Oxynitride Nanoribbons with Anion Exchange. *ACS Nano* **2015**, *9* (10), 10133–10141. <https://doi.org/10.1021/acs.nano.5b03742>.
- (48) Andersson, S.; Collén, B.; Kuylenstierna, U.; Magnéli, A.; Magnéli, A.; Pestmalis, H.; Åsbrink, S. Phase Analysis Studies on the Titanium-Oxygen System. *Acta Chem. Scand.* **1957**, *11*, 1641–1652. <https://doi.org/10.3891/acta.chem.scand.11-1641>.
- (49) Milošev, I.; Strehblow, H.-H.; Navinšek, B. Comparison of TiN, ZrN and CrN Hard Nitride Coatings: Electrochemical and Thermal Oxidation. *Thin Solid Films* **1997**, *303* (1), 246–254. [https://doi.org/10.1016/S0040-6090\(97\)00069-2](https://doi.org/10.1016/S0040-6090(97)00069-2).
- (50) Ernsberger, C.; Nickerson, J.; Smith, T.; Miller, A. E.; Banks, D. Low Temperature Oxidation Behavior of Reactively Sputtered TiN by X-ray Photoelectron Spectroscopy and Contact Resistance Measurements. *J. Vac. Sci. Technol. A* **1986**, *4* (6), 2784–2788. <https://doi.org/10.1116/1.573679>.
- (51) Meng, L.-J.; Santos, M. P. dos. Characterization of Titanium Nitride Films Prepared by d.c. Reactive Magnetron Sputtering at Different Nitrogen Pressures. *Surf. Coat. Technol.* **1997**, *90* (1), 64–70. [https://doi.org/10.1016/S0257-8972\(96\)03094-0](https://doi.org/10.1016/S0257-8972(96)03094-0).
- (52) Braic, L.; Vasilantonakis, N.; Mihai, A.; Villar Garcia, I. J.; Fearn, S.; Zou, B.; Alford, N. McN.; Doiron, B.; Oulton, R. F.; Maier, S. A.; Zayats, A. V.; Petrov, P. K. Titanium Oxynitride Thin Films with Tunable Double Epsilon-Near-Zero Behavior for Nanophotonic Applications. *ACS Appl. Mater. Interfaces* **2017**, *9* (35), 29857–29862. <https://doi.org/10.1021/acsami.7b07660>.
- (53) Quijorna, E. P.; Costa, V. T.; Agulló-Rueda, F.; Fernández, P. H.; Climent, A.; Rossi, F.; Silván, M. M. TiN_xO_y/TiN Dielectric Contrasts Obtained by Ion Implantation of O²⁺; Structural, Optical and Electrical Properties. *J. Phys. Appl. Phys.* **2011**, *44* (23), 235501. <https://doi.org/10.1088/0022-3727/44/23/235501>.
- (54) Yamaguchi, M.; Ishii, A.; Oikawa, I.; Takamura, H. Black Titanium Oxynitride Thin Films Prepared by Nitrogen Plasma-Assisted Pulsed Laser Deposition for Flat-Panel Displays. *Appl. Surf. Sci.* **2020**, *534*, 147616. <https://doi.org/10.1016/j.apsusc.2020.147616>.
- (55) Prodan, E.; Radloff, C.; Halas, N. J.; Nordlander, P. A Hybridization Model for the Plasmon Response of Complex Nanostructures. *Science* **2003**, *302* (5644), 419–422. <https://doi.org/10.1126/science.1089171>.
- (56) Lassiter, J. B.; Aizpurua, J.; Hernandez, L. I.; Brandl, D. W.; Romero, I.; Lal, S.; Hafner, J. H.; Nordlander, P.; Halas, N. J. Close Encounters between Two Nanoshells. *Nano Lett.* **2008**, *8* (4), 1212–1218. <https://doi.org/10.1021/nl080271o>.
- (57) Rinnerbauer, V.; Lenert, A.; Bierman, D. M.; Yeng, Y. X.; Chan, W. R.; Geil, R. D.; Senkevich, J. J.; Joannopoulos, J. D.; Wang, E. N.; Soljačić, M.; Celanovic, I. Metallic Photonic Crystal Absorber-Emitter for Efficient Spectral Control in High-Temperature Solar Thermophotovoltaics. *Adv. Energy Mater.* **2014**, *4* (12), 1400334. <https://doi.org/10.1002/aenm.201400334>.
- (58) Li, Y.; Li, D.; Zhou, D.; Chi, C.; Yang, S.; Huang, B. Efficient, Scalable, and High-Temperature Selective Solar Absorbers Based on Hybrid-Strategy Plasmonic Metamaterials. *Sol. RRL* **2018**, *2* (8), 1800057. <https://doi.org/10.1002/solr.201800057>.
- (59) Gao, H.; Peng, W.; Cui, W.; Chu, S.; Yu, L.; Yang, X. Ultraviolet to near Infrared Titanium Nitride Broadband Plasmonic Absorber. *Opt. Mater.* **2019**, *97*, 109377. <https://doi.org/10.1016/j.optmat.2019.109377>.

- (60) Guler, U.; Kildishev, A. V.; Boltasseva, A.; Shalaev, V. M. Plasmonics on the Slope of Enlightenment: The Role of Transition Metal Nitrides. *Faraday Discuss.* **2015**, *178* (0), 71–86. <https://doi.org/10.1039/C4FD00208C>.
- (61) Goya, S.; Murai, S.; Tanaka, K. Thermal Oxidation of TiN Nanocylinder Arrays: Effects of Insulator Coatings by Atomic Layer Deposition. *Opt. Mater. Express* **2019**, *9* (12), 4751–4764. <https://doi.org/10.1364/OME.9.004751>.
- (62) Mutlu, M.; Kang, J.-H.; Raza, S.; Schoen, D.; Zheng, X.; Kik, P. G.; Brongersma, M. L. Thermoplasmonic Ignition of Metal Nanoparticles. *Nano Lett.* **2018**, *18* (3), 1699–1706. <https://doi.org/10.1021/acs.nanolett.7b04739>.
- (63) Passoni, L.; Criante, L.; Fumagalli, F.; Scotognella, F.; Lanzani, G.; Di Fonzo, F. Self-Assembled Hierarchical Nanostructures for High-Efficiency Porous Photonic Crystals. *ACS Nano* **2014**, *8* (12), 12167–12174. <https://doi.org/10.1021/nn5037202>.
- (64) Guler, U.; Zemlyanov, D.; Kim, J.; Wang, Z.; Chandrasekar, R.; Meng, X.; Stach, E.; Kildishev, A. V.; Shalaev, V. M.; Boltasseva, A. Plasmonic Titanium Nitride Nanostructures via Nitridation of Nanopatterned Titanium Dioxide. *Adv. Opt. Mater.* **2017**, *5* (7), 1600717. <https://doi.org/10.1002/adom.201600717>.